

# Real-time 3-D modeling of the ground electric field due to space weather events. A concept and its validation

Mikhail Kruglyakov<sup>1,2</sup>, Alexey Kuvshinov<sup>3</sup>, Elena Marshalko<sup>4,5</sup>

<sup>1</sup>University of Otago, Dunedin, New Zealand

<sup>2</sup>Geoelectromagnetic Research Center, Institute of Physics of the Earth, Moscow, Russia

<sup>3</sup>Institute of Geophysics, ETH Zürich, Zürich, Switzerland

<sup>4</sup>Institute of Physics of the Earth, Moscow, Russia

<sup>5</sup>Geophysical Center, Moscow, Russia

## Key Points:

- We present the formalism of real-time modeling of the ground electric field (GEF) excited by temporally and spatially varying source
- The formalism relies on the factorization of the source and exploits precomputed frequency-domain GEF
- Using Fennoscandia as a test region, we show that real-time 3-D modeling of the GEF takes less than 0.025 seconds

---

Corresponding author: Mikhail Kruglyakov, [m.kruglyakov@gmail.com](mailto:m.kruglyakov@gmail.com)

## Abstract

We present a methodology that allows researchers to simulate in real time the spatiotemporal dynamics of the ground electric field (GEF) in a given 3-D conductivity model of the Earth based on continuously augmented data on the spatiotemporal evolution of the inducing source. The formalism relies on the factorization of the source by spatial modes and time series of respective expansion coefficients and exploits precomputed frequency-domain GEF generated by corresponding spatial modes. To validate the formalism, we invoke a high-resolution 3-D conductivity model of Fennoscandia and consider a realistic source built using the Spherical Elementary Current Systems (SECS) method as applied to magnetic field data from the IMAGE network of observations. The factorization of the SECS-recovered source is then performed using the principal component analysis. Eventually, we show that the GEF computation at a given time instant on a  $512 \times 512$  grid requires less than 0.025 seconds provided that frequency-domain GEF due to pre-selected spatial modes are computed in advance. Taking the 7-8 September 2017 geomagnetic storm as a space weather event, we show that real-time high-resolution 3-D modeling of the GEF is feasible.

## Plain Language Summary

The solar activity in the form of coronal mass ejections leads to abnormal fluctuations of the geomagnetic field. These fluctuations, in their turn, generate so-called geomagnetically induced currents (GIC) in electrical grids, which may pose a significant risk to the reliability and durability of such infrastructure. Forecasting GIC is one of the grand challenges of modern space weather studies. One of the critical components of such forecasting is real-time simulation of the ground electric field (GEF), which depends on the electrical conductivity distribution inside the Earth and the spatiotemporal structure of geomagnetic field fluctuations. In this paper, we present and validate a methodology that allows researchers to simulate the GEF in fractions of a second (thus, in real time) irrespective of the complexity of the conductivity and geomagnetic field fluctuations models.

## 1 Introduction

As commonly recognized, geomagnetically induced currents (GIC) in power electric grids may pose a significant risk to the reliability and durability of such infrastructure (Bolduc, 2002; Love et al., 2018).

The ultimate goal of quantitative estimation of the hazard to power grids from abnormal geomagnetic disturbances (space weather events) is real-time and as realistic as practicable forecasting of GIC. Under GIC forecasting, we understand the time-domain computation of GIC using continuously augmented data on the spatiotemporal evolution of the source responsible for the geomagnetic disturbances. Specifically, to forecast GIC in the region of interest, one needs: (1) to adequately parameterize the source of geomagnetic disturbances; (2) to forecast the spatiotemporal evolution of the source in the region; (3) to specify/build a three-dimensional (3-D) electrical conductivity model of the Earth's subsurface; (4) to perform real-time modeling of the ground electric field (GEF) in a given 3-D conductivity model, i.e., to compute as fast as feasible the spatiotemporal progression of the GEF from continuously augmented data on the spatiotemporal evolution of the forecasted source; (5) to convert the "forecasted" GEF into GIC.

It is well accepted that the decades of satellite observations of the solar wind parameters (plus observations of interplanetary magnetic field) at the L1 Lagrangian point are the most promising data for forecasting spatiotemporal evolution of the source with algorithms known as neural networks (NN). Despite numerous studies that attempt to forecast the source evolution using different NN architectures quantitatively, the progress

65 here is rather limited. This is, in particular, because the full potential of NN remains  
 66 unexplored; the reader can find a rather exhaustive review of the literature on the sub-  
 67 ject in Tasistro-Hart et al. (2021). But even if the source forecasting will be feasible in  
 68 the future, with the measurements at the L1 point, it is nearly impossible to forecast the  
 69 source more than an hour in advance. This, in particular, means that forecasting GEF  
 70 in a given 3-D conductivity model from continuously augmented data on the spatiotem-  
 71 poral evolution of the forecasted source should be performed “on the fly”, i.e., within a  
 72 few seconds, if one wishes to approach an ultimate goal of GIC forecasting in the region  
 73 of interest – development of trustful alerting systems for the power industry. Note that  
 74 once the GEF is forecasted, a conversion of the GEF into GIC is rather straightforward  
 75 (Kelbert, 2020) and requires fractions of seconds provided the geometry of transmission  
 76 lines and system design parameters are granted by power companies.

77 This paper presents and validates a methodology that allows researchers to sim-  
 78 ulate the spatiotemporal progression of the GEF in a 3-D conductivity model “on the  
 79 fly”.

## 80 2 Methodology

### 81 2.1 Governing equations in the frequency domain

82 We start with the discussion of the problem in the frequency domain. Maxwell’s  
 83 equations govern electromagnetic (EM) field variations, and in the frequency domain,  
 84 these equations are read as

$$\frac{1}{\mu_0} \nabla \times \mathbf{B} = \sigma \mathbf{E} + \mathbf{j}^{\text{ext}}, \quad (1)$$

$$\nabla \times \mathbf{E} = i\omega \mathbf{B}, \quad (2)$$

where  $\mu_0$  is the magnetic permeability of free space;  $\omega$  is angular frequency;  $\mathbf{j}^{\text{ext}}(\mathbf{r}, \omega)$   
 is the extraneous (inducing) electric current density;  $\mathbf{B}(\mathbf{r}, \omega; \sigma)$ ,  $\mathbf{E}(\mathbf{r}, \omega; \sigma)$  are magnetic  
 and electric fields, respectively.  $\sigma(\mathbf{r})$  is the spatial distribution of electrical conductiv-  
 ity,  $\mathbf{r} = (r, \vartheta, \varphi)$  a position vector, either in the spherical or Cartesian coordinates. Note  
 that we neglected displacement currents and adopt the following Fourier convention

$$f(t) = \frac{1}{2\pi} \int_{-\infty}^{\infty} \tilde{f}(\omega) e^{-i\omega t} d\omega. \quad (3)$$

85 We also assume that the current density,  $\mathbf{j}^{\text{ext}}(\mathbf{r}, \omega)$ , can be represented as a linear com-  
 86 bination of spatial modes  $\mathbf{j}_i(\mathbf{r})$ ,

$$\mathbf{j}^{\text{ext}}(\mathbf{r}, \omega) = \sum_{i=1}^L c_i(\omega) \mathbf{j}_i(\mathbf{r}). \quad (4)$$

87 Note that the form of spatial modes  $\mathbf{j}_i(\mathbf{r})$  (and their number,  $L$ ) varies with application.  
 88 For example,  $\mathbf{j}^{\text{ext}}(\mathbf{r}, \omega)$  is parameterized via spherical harmonics (SH) in Püthe and Ku-  
 89 vshinov (2013); Honkonen et al. (2018); Guzavina et al. (2019); Grayver et al. (2021),  
 90 current loops in Sun and Egbert (2012), or eigenmodes from the PCA analysis of the physics-  
 91 based models in Egbert et al. (2021); Zenhausern et al. (2021).

By virtue of the linearity of Maxwell’s equations with respect to the  $\mathbf{j}^{\text{ext}}(\mathbf{r}, \omega)$  term,  
 we can expand the total (i.e., inducing plus induced) electric field as a linear combina-  
 tion of individual fields  $\mathbf{E}_i$ ,

$$\mathbf{E}(\mathbf{r}, \omega; \sigma) = \sum_{i=1}^L c_i(\omega) \mathbf{E}_i(\mathbf{r}, \omega; \sigma), \quad (5)$$

92 where the  $\mathbf{E}_i(\mathbf{r}, \omega; \sigma)$  field is the “electric” solution of the following Maxwell’s equations

$$\frac{1}{\mu_0} \nabla \times \mathbf{B}_i = \sigma \mathbf{E}_i + \mathbf{j}_i, \quad (6)$$

$$\nabla \times \mathbf{E}_i = i\omega \mathbf{B}_i. \quad (7)$$

## 93 2.2 Governing equations in the time domain

The transformation of the Equation (5) into the time domain leads to the representation of the time-varying ground electric field as convolution integrals

$$\mathbf{E}(\mathbf{r}_s, t; \sigma) = \sum_{i=1}^L \int_{-\infty}^t c_i(\tau) \mathbf{E}_i(\mathbf{r}_s, t - \tau; \sigma) d\tau, \quad (8)$$

or equivalently

$$\mathbf{E}(\mathbf{r}_s, t; \sigma) = \sum_{i=1}^L \int_0^{\infty} c_i(t - \tau) \mathbf{E}_i(\mathbf{r}_s, \tau; \sigma) d\tau, \quad (9)$$

94 where  $\mathbf{r}_s$  stands for the position vector at the surface of the Earth. The reader is referred  
95 to Appendix A for more details on the convolution integrals in Equations (8) and (9).

96 Since the radial component of the GEF is negligibly small (due to insulating air)  
97 and is not used in GIC calculations (Kelbert, 2020), we will confine ourselves to forecast-  
98 ing of the horizontal electric field solely; thus, hereinafter,  $\mathbf{E}_i$  will stand for  $\mathbf{E}_i = (E_{x,i} \ E_{y,i})$ .

## 99 2.3 Real-time modeling of the GEF. A concept

Equation (9) shows how the GEF can be modeled using continuously augmented data on the time evolution of the nowcasted or forecasted  $c_i$  (note that forecasting of the  $c_i$  is outside the scope of this paper). To make the formula ready for implementation, one needs: (a) to specify a set of spatial modes,  $\mathbf{j}_i, i = 1, 2, \dots, L$  in the region, where GIC nowcasting/forecasting is required; we will discuss the construction of  $\mathbf{j}_i$  in Section 3.1; (b) to set up a 3-D conductivity model in this region; and (c) to estimate an upper limit of integrals in Equation (9), or, in other words, to estimate a time interval,  $T$ , above which  $\mathbf{E}_i(\mathbf{r}_s, \tau; \sigma)$  becomes negligibly small. The latter will allow us to rewrite Equation (9) as

$$\mathbf{E}(\mathbf{r}_s, t; \sigma) \approx \sum_{i=1}^L \int_0^T c_i(t - \tau) \mathbf{E}_i(\mathbf{r}_s, \tau; \sigma) d\tau. \quad (10)$$

100 Note that the upper limit in the integrals could be different for different spatial modes,  
101 different components of the field, and different locations. However, one can choose a con-  
102 servative approach, taking a single  $T$  irrespective of modes/components/locations as a  
103 maximum from all individual upper limit estimates. We will discuss the estimation of  
104  $T$  in Sections 3.3 and 3.4 .

The details of numerical calculation of the integrals in (10) are presented in Appendix B. In short, assuming that  $c_i(t), i = 1, 2, \dots, L$  are time series with the sampling interval  $\Delta t$  and  $T = N_t \Delta t$ , we approximate  $\mathbf{E}(\mathbf{r}_s, t_k; \sigma)$  at  $t_k = k \Delta t$  as

$$\mathbf{E}(\mathbf{r}_s, t_k; \sigma) \approx \sum_{i=1}^L \left\{ \sum_{n=0}^{N_t} d_i(t_k, n \Delta t; T) G_{\mathbf{E}_i}^n(\mathbf{r}_s; \sigma) + [c_i(t_k - T) - c_i(t_k)] L_i(\mathbf{r}_s, T; \sigma) \right\}, \quad (11)$$

where  $d_i$  is defined as

$$d_i(t, \tau; T) = \begin{cases} c_i(t - \tau) - c_i(t) - \frac{c_i(t - T) - c_i(t)}{T} \tau, & \tau \in [0, T] \\ 0, & \tau \notin [0, T]. \end{cases} \quad (12)$$

105 The reasoning to represent time-dependent part in Equation (11) in this form is given  
 106 in Appendix B. Note also that quantities  $G_{\mathbf{E}_i}^n(\mathbf{r}_s; \sigma)$  and  $L_i(\mathbf{r}_s, T; \sigma)$  are time-invariant,  
 107 and for the given  $\mathbf{j}_i$ ,  $i = 1, 2, \dots, L$  and 3-D conductivity model are calculated only once,  
 108 then stored and used, when the calculation of  $\mathbf{E}(\mathbf{r}_s, t_k; \sigma)$  is required. Actual form and  
 109 estimation for  $G_{\mathbf{E}_i}^n(\mathbf{r}_s; \sigma)$  and  $L_i(\mathbf{r}_s, T; \sigma)$  are also discussed in Appendix B.

110 Equation (11) is an essence of the real-time GEF calculation, showing that  $\mathcal{O}(L \times N_t \times N_g)$   
 111 summations and multiplications are required at a (current) time instant  $t_k$  plus some over-  
 112 head to read the precomputed  $G_{\mathbf{E}_i}^n(\mathbf{r}_s; \sigma)$  and  $L_i(\mathbf{r}_s, T; \sigma)$  from the disc. Note that  $N_g$   
 113 is a number of points  $\mathbf{r}_s$ , at which the GEF is computed.

### 114 3 Real-time modeling of the GEF. Validation of the concept

115 The validation of the presented concept will be performed using Fennoscandia as  
 116 a test region. The choice of Fennoscandia is motivated by several reasons. First, it is a  
 117 high-latitude region, where GIC are expected to be especially large. Second, there ex-  
 118 ists a 3-D electrical conductivity model of the region (Korja et al., 2002). Third, the re-  
 119 gional magnetometer network (International Monitor for Auroral Geomagnetic Effect,  
 120 IMAGE (Tanskanen, 2009), allows us to build a realistic model of the source. Finally,  
 121 the last but not the least consideration to choose this region is the fact that we have al-  
 122 ready performed a comprehensive 3-D EM model study in this region (Marshalko et al.,  
 123 2021).

#### 124 3.1 Building a model of the source

125 First, let us rewrite Equation (4) in the time domain

$$\mathbf{j}^{\text{ext}}(\mathbf{r}, t) = \sum_{i=1}^L c_i(t) \mathbf{j}_i(\mathbf{r}). \quad (13)$$

126 We will further assume that the extraneous current  $\mathbf{j}^{\text{ext}}(\mathbf{r}, t)$  is divergence-free, it flows  
 127 in a thin layer at the altitude of  $h = 90$  km, and this layer is separated from the Earth  
 128 by the insulating atmosphere. Following the Spherical Elementary Current Systems (SECS)  
 129 method (Vanhamäki & Juusola, 2020), this current is represented as

$$\mathbf{j}^{\text{ext}}(\mathbf{r}, t) = \delta(r - R) \sum_{m=1}^M S_m(t) [P(\mathbf{r}, \mathbf{r}_m) \mathbf{e}_\vartheta + Q(\mathbf{r}, \mathbf{r}_m) \mathbf{e}_\varphi], \quad (14)$$

where  $\delta$  is Dirac's delta function,  $\mathbf{e}_\vartheta$  and  $\mathbf{e}_\varphi$  are unit vectors of the spherical coordinate system,  $\mathbf{r} = (R, \vartheta, \varphi)$ ,  $\mathbf{r}_m = (R, \vartheta_m, \varphi_m)$ ,  $R = a + h$ ,  $a$  is a mean radius of the Earth,  $\mathbf{r}_m$  is the location of the pole of the  $m$ -th spherical elementary current system and  $S_m$  is the so-called scalar factor associated with the  $m$ -th pole. Expressions for  $P(\mathbf{r}, \mathbf{r}_m)$  and  $Q(\mathbf{r}, \mathbf{r}_m)$  are presented in Appendix D. Note that in practice  $\mathbf{r}$  and  $\mathbf{r}_m$  are usually taken as the nodes of two (similar) grids, which are slightly shifted with respect to each other (the reason for the shift is explained in Appendix D). Once  $S_m(t)$ ,  $m = 1 \dots M$  are obtained by means of the SECS method as applied to some real data for some event, one can perform the PCA of  $S_m(t)$  expecting that the spatial structure of  $S_m(t)$  will be well approximated with a small number of modes  $v_i$ ,  $i = 1, 2, \dots, L$  allowing to represent  $\mathbf{j}_i$  as

$$\mathbf{j}_i(\mathbf{r}) = \delta(r - R) \sum_{m=1}^M v_i(\mathbf{r}_m) [P(\mathbf{r}, \mathbf{r}_m) \mathbf{e}_\vartheta + Q(\mathbf{r}, \mathbf{r}_m) \mathbf{e}_\varphi], \quad i = 1, 2, \dots, L. \quad (15)$$

130 The aim of this section is to obtain  $v_i$  and, consequently,  $\mathbf{j}_i$  (using Equation 15). To this  
 131 end, we apply the SECS method to 10-sec vector magnetic field data from all available (38)  
 132 stations of the IMAGE network during the 7-8 September 2017 geomagnetic storm. Lo-  
 133 cations of IMAGE sites are shown in Figure 1. Considered (8-hours) time period is from

134 20:00:00 UT, September 7, 2017, to 03:59:50 UT, September 8, 2017, thus, including the  
 135 onset and the main phase of the storm.  $S$  was estimated at  $0.5^\circ \times 1^\circ$  grid of  $21^\circ \times 38^\circ$   
 136 part of a sphere. Coordinates of the region are  $59^\circ\text{N} - 79^\circ\text{N}$  and  $4^\circ\text{E} - 42^\circ\text{E}$ . This set  
 137 up, in particular, means that  $S$  was computed at  $M = 42 \times 39 = 1638$  grid points  
 138 and  $N = 2880$  time instants. Note that the same event, region and grid were consid-  
 139 ered in our recent study (Marshalko et al., 2021).

The PCA of  $S_m(t)$  is performed in a similar manner as it was done, for example,  
 in Alken et al. (2017); Egbert et al. (2021); Zenhausern et al. (2021). Specifically, we con-  
 struct a matrix  $F$  as

$$F = \begin{pmatrix} S_1^1 & S_2^1 & \cdots & S_M^1 \\ S_1^2 & S_2^2 & \cdots & S_M^2 \\ \vdots & \vdots & \ddots & \vdots \\ S_1^N & S_2^N & \cdots & S_M^N \end{pmatrix}, \quad (16)$$

where  $S_m^n$  is  $S_m(t)$  estimated at the  $n$ -th time instant at the  $m$ -th grid point. Further,  
 according to the PCA concept, we form an  $M \times M$  covariance matrix  $R$

$$R = F^T F, \quad (17)$$

and apply an eigenvalue decomposition to  $R$

$$R V = \Lambda V, \quad (18)$$

where  $\Lambda$  is a diagonal matrix containing the eigenvalues  $\lambda_i, i = 1, 2, \dots, M$  of  $R$ . The  
 $v_i$  column vector of  $V$  is the eigenvector of  $R$  corresponding to the eigenvalue  $\lambda_i$ . Both  
 $V$  and  $\Lambda$  are matrices of the size  $M \times M$ . The superscript  $T$  in Equation (17) denotes  
 the transpose. The eigenvectors  $v_i$  represent the spatial modes (principal components;  
 PCs), whereas the eigenvalues give the respective PC's variance contribution. The cor-  
 responding time series  $c_i$  are calculated as

$$c_i = F v_i. \quad (19)$$

PCs are usually sorted in order from the largest to the smallest eigenvalues. The PC cor-  
 responding to the largest eigenvalue will explain the most variance, followed by the sec-  
 ond, third PC, etc... In practice, the PCs corresponding to a few of the largest eigen-  
 values explain most of the analyzed fields' variance. The cumulative variance of  $L$  PCs  
 can be calculated as (Alken et al., 2017)

$$\kappa_L = \frac{\sum_{i=1}^L \lambda_i}{\sum_{i=1}^M \lambda_i}, \quad (20)$$

140 Figure 2 presents the cumulative variance for the first 30 spatial modes. Horizontal dashed  
 141 line allows us to estimate the number of modes needed to explain 99 % of the spatial vari-  
 142 ability of  $S_m(t)$ . It is seen from the figure that one needs  $L = 21$  spatial modes to ex-  
 143 plain most (99 %) of the variance. This is a dramatic reduction from the total  $M = 1638$   
 144 spatial modes. These 21 modes will be used in the further discussion of the real-time cal-  
 145 culation of the GEF. Figure 3 shows  $\mathbf{j}_i$  corresponding to spatial modes of different  $i$ , il-  
 146 lustrating the fact that the modes with larger  $i$  capture smaller spatial structures of the  
 147 source. The respective time series  $c_i$  are presented in Figure 4. Figure 5 compares the  
 148 maps of the original and the PCA-based source for two snapshots of the enhanced geo-  
 149 magnetic activity. The original source is built using the SECS method (cf. Equation 14),  
 150 whereas PCA-based source is calculated using Equations (13) and (15). It is seen that  
 151 the agreement between the original and PCA-based sources is very good both in terms

of the amplitude and spatial pattern. In addition, Figure 6 demonstrates the comparison of the time series of these sources for two exemplary sites (shown in Figure 5 as white circles): one is located in the region where the significant source current is observed, another – aside from this region. Again, we observe good agreement between the two sources, especially for the site above which the source current is large.

### 3.2 3-D conductivity model of Fennoscandia

We took the 3-D conductivity model of the region from Marshalko et al. (2021), where it was constructed using the SMAP (Korja et al., 2002) – a set of maps of crustal conductances (vertically integrated electrical conductivities) of the Fennoscandian Shield, surrounding seas, and continental areas. The SMAP consists of six layers of laterally variable conductance. Each layer has a thickness of 10 km. The first layer comprises contributions from the seawater, sediments, and upper crust. The other five layers describe conductivity distribution in the middle and lower crust. SMAP covers an area  $0^\circ\text{E} - 50^\circ\text{E}$  and  $50^\circ\text{N} - 85^\circ\text{N}$  and has  $5' \times 5'$  resolution. We converted the original SMAP database into a Cartesian 3-D conductivity model of Fennoscandia with three layers of laterally variable conductivity of 10, 20, and 30 km thicknesses (Figures 7.a-c). This vertical discretization is chosen to be compatible with that previously used by Rosenqvist and Hall (2019) and Dimmock et al. (2019, 2020) for GIC studies in the region. Conductivities in the second and the third layer of this model are simple averages of the conductivities in the corresponding layers of the original conductivity model with six layers. To obtain the conductivities in Cartesian coordinates, we applied the transverse Mercator map projection (latitude and longitude of the true origin are  $50^\circ\text{N}$  and  $25^\circ\text{E}$ , correspondingly) to the original data, and then performed the interpolation to a laterally regular grid. The lateral discretization and the size of the resulting 3-D part of the conductivity model of Fennoscandia were taken as  $5 \times 5 \text{ km}^2$  and  $2550 \times 2550 \text{ km}^2$ , respectively. Deeper than 60 km, we used the 1-D conductivity profile obtained by Kuvshinov et al. (2021) (cf. Figure 7.d), which is an updated version of the 1-D profile from Grayver et al. (2017).

Note that the lateral discretization and the size of the conductivity model of Fennoscandia imply that the GEF is calculated at a grid comprising  $N_g = 512 \times 512$  points.

### 3.3 Computation of $\mathbf{E}_i(\mathbf{r}_s, \omega; \sigma)$

As is seen from Equations (B13) and (C2) one needs to compute  $\mathbf{E}_i(\mathbf{r}_s, \omega; \sigma)$  at a number of frequencies, or, in other words, to solve Maxwell’s equations (6). These equations are numerically solved using the 3-D EM forward modeling code PGIEM2G (Kruglyakov & Kuvshinov, 2018), which is based on a method of volume integral equations (IE) with a contracting kernel (Pankratov & Kuvshinov, 2016). PGIEM2G exploits a piece-wise polynomial basis; in this study, PGIEM2G was run using the first-order polynomials in lateral directions and third-order polynomials in the vertical direction.

Figures 11, 12, and 13 demonstrate  $\mathbf{E}_i(\mathbf{r}_s, \omega; \sigma)$  at observatories Abisko (ABK), Uppsala (UPS), and Saint Petersburg (SPG), respectively. The results are for the excitations corresponding to the first, seventh, fourteenth and twenty-first spatial modes and are shown for the frequency range from  $10^{-5}$  Hz to 1 Hz. From these figures, a few observations can be made. The behavior of  $\mathbf{E}_i$  (with respect to frequency) varies with location and mode. Real and imaginary parts of  $\mathbf{E}_i$  are comparable in magnitude. As expected,  $\mathbf{E}_i$  are smooth functions with respect to the frequency; apparent non-smoothness of the results in some plots is due to the fact that *absolute* values of real and imaginary parts are shown.

Finally, it is important to note that  $\mathbf{E}_i$  decrease – irrespective of the mode and location – as frequency decreases; specifically, the magnitude of  $\mathbf{E}_i$  drops down more than two orders of magnitude as frequency decreases from 1 Hz down to  $10^{-3}$  Hz. These plots

201 suggest a value for  $T$  in Equation (10); recall, that useful rule of thumb is that the value  
 202 for  $T$  corresponds to the inverse of frequency at which the field becomes small compared  
 203 to the higher frequencies. Following this rule,  $T = 1000$  seconds seems to be a reason-  
 204 able choice which will be further justified in the next section.

### 205 3.4 Model study to justify a value for $T$

206 First, we calculate time-domain electric field for a chosen 8-hours event using a nu-  
 207 merical scheme presented in Ivannikova et al. (2018); Marshalko et al. (2020, 2021). Specif-  
 208 ically, we calculate  $\mathbf{j}^{ext}(t, \mathbf{r})$  using Equations (13) and (15) and taking 21 terms in ex-  
 209 pansion (13). Further, according to Marshalko et al. (2021), we calculate the electric field  
 210 as follows:

- 211 1. The source  $\mathbf{j}^{ext}(t, \mathbf{r})$  is transformed from the time to the frequency domain with  
 212 a fast Fourier transform (FFT).
- 213 2. Frequency-domain Maxwell's equations (1)-(2) are numerically solved using PGIEM2G  
 214 at FFT frequencies between  $\frac{1}{K}$  and  $\frac{1}{2\Delta t}$  where  $K$  is the length of the event, and  
 215  $\Delta t$  is the sampling rate of the considered time series. In this study  $\Delta t$  is 10 sec,  
 216 and  $K$  is 8 h.
- 217 3.  $\mathbf{E}(t, \mathbf{r})$  is obtained with an inverse FFT of the frequency-domain field.

218 Electric field calculated using the above scheme is considered as a reference (“true”) so-  
 219 lution. We also calculate electric field using Equation (11) with  $T = 900$  sec (15 min)  
 220 and with  $T = 3600$  sec (1 hour).

Figures 11, 12, and 13 show electric field time series modeled at three geomagnetic  
 observatories. Comparison is between the reference GEF and GEF modeled using the  
 “real-time” scheme. It is seen that both “real-time” (either calculated using  $T = 15$   
 min or  $T = 1$  h) electric fields agree well with the reference electric field. Table 1 con-  
 firms this quantitatively by presenting correlation coefficients between corresponding time  
 series and the normalized root-mean-square errors, which are defined as

$$\text{nRMSE}(a, b) = \sqrt{\frac{\sum_{i=1}^N (a_i - b_i)^2}{N}} / \sqrt{\frac{\sum_{i=1}^N b_i^2}{N}}, \quad (21)$$

221 where  $a$  and  $b$  are the reference GEF time series and GEF time series calculated exploit-  
 222 ing real-time scheme, respectively,  $a_i$  and  $b_i$  are elements of these time series, and  $N$  is  
 223 the number of time instants. Since results for  $T = 15$  min and  $T = 1$  h appear to be  
 224 very similar, we present in the next section the estimates of computational loads for the  
 225 case when  $T$  is taken as 15 min.

### 226 3.5 Computational loads for the real-time GEF calculation

227 Once  $G_{\mathbf{E}_i}^n(\mathbf{r}_s; \sigma)$  and  $L_i(\mathbf{r}_s, T; \sigma)$  are computed and stored on the disc, GEF at a  
 228 grid  $N_x \times N_y$  and time instant  $t_k$  is computed using Equation (11). In accordance with  
 229 this equation, the GEF calculation requires forecasting/nowcasting the  $L \times N_t$  array  $c$ ,  
 230 reading the  $L \times N_t \times N_g$  array  $G_{\mathbf{E}_i}^n$  and  $L \times N_g$  array  $L_i$ , and performing  $\mathcal{O}(L \times N_t \times N_g)$   
 231 summations and multiplications. For our problem setup with  $N_g = 512 \times 512$ ,  $N_t =$   
 232 90 and  $L = 21$  the calculation of  $\mathbf{E}(\mathbf{r}_s, t_k; \sigma)$  takes from 0.00625 to 0.025 seconds, de-  
 233 pending on the computational environment. Note that to store arrays for this setup one  
 234 needs 7.25 Gigabytes of disc space.

## 4 Conclusions

In this paper, we presented a formalism for the real-time computation of the ground electric field (GEF) in a given 3-D Earth's conductivity model excited by a continuously augmented spatially- and temporally-varying source responsible for a space weather event.

The formalism relies on a factorization of the source by spatial modes and time series of respective expansion coefficients, and exploits precomputed frequency-domain GEF generated by corresponding spatial modes.

To validate the formalism, we invoked a high-resolution 3-D conductivity model of Fennoscandia and considered a realistic source built with the use of the SECS method as applied to magnetic field data from the IMAGE network of observations. Factorization of the SECS-recovered source is then performed using the principal component analysis. Eventually, we show that the GEF computation at a given time instant on a  $512 \times 512$  grid requires at most 0.025 seconds provided that frequency-domain GEF due to the pre-selected spatial modes are computed in advance. This opens a practical opportunity for GEF forecasting, using, for example, L1 data.

We illustrate the concept on a Cartesian geometry problem setup. Global-scale implementation is rather straightforward; for this scenario, the source could be obtained either using magnetic field data from a global network of observatories or exploiting the results of the first-principle modeling of the global magnetosphere-ionosphere system.

## Acknowledgments

MK was supported by the New Zealand Ministry of Business, Innovation & Employment through Endeavour Fund Research Programme contract UOOX2002. EM has been supported by grant 21-77-30010 from the Russian Science Foundation. AK was supported in the framework of Swarm DISC activities, funded by ESA contract no. 4000109587, with the support from EO Science for Society. The SMAP model is available via the EPOS portal ([http://mt.bgs.ac.uk/EPOSMT/2019/MOD/EPOSMT2019\\_3D.mod.json](http://mt.bgs.ac.uk/EPOSMT/2019/MOD/EPOSMT2019_3D.mod.json)). We thank the institutes that maintain the IMAGE Magnetometer Array: Tromsø Geophysical Observatory of UiT, the Arctic University of Norway (Norway), Finnish Meteorological Institute (Finland), Institute of Geophysics Polish Academy of Sciences (Poland), GFZ German Research Center for Geosciences (Germany), Geological Survey of Sweden (Sweden), Swedish Institute of Space Physics (Sweden), Sodankylä Geophysical Observatory of the University of Oulu (Finland), and Polar Geophysical Institute (Russia). We thank INTERMAGNET ([www.intermagnet.org](http://www.intermagnet.org)) for promoting high standards of magnetic observatory practice.

## References

- Alken, P., Maute, A., Richmond, A. D., Vanhamäki, H., & Egbert, G. D. (2017). An application of principal component analysis to the interpretation of ionospheric current systems. *Journal of Geophysical Research: Space Physics*, *122*(5), 5687–5708. doi: 10.1002/2017JA024051
- Bolduc, L. (2002). GIC observations and studies in the Hydro-Québec power system. *Journal of Atmospheric and Solar-Terrestrial Physics*, *64*(16), 1793–1802. (Space Weather Effects on Technological Systems) doi: 10.1016/S1364-6826(02)00128-1
- Dimmock, A. P., Rosenqvist, L., Hall, J.-O., Viljanen, A., Yordanova, E., Honkonen, I., ... Sjöberg, E. C. (2019). The GIC and geomagnetic response over Fennoscandia to the 7-8 September 2017 geomagnetic storm. *Space Weather*, *17*(7), 989–1010. doi: 10.1029/2018SW002132
- Dimmock, A. P., Rosenqvist, L., Welling, D., Viljanen, A., Honkonen, I., Boynton, R. J., & Yordanova, E. (2020). On the regional variability of dB/dt

- 284 and its significance to GIC. *Space Weather*, 18, e2020SW002497. doi:  
285 10.1029/2020SW002497
- 286 Egbert, G. D., Alken, P., Maute, A., Zhang, H., & Richmond, A. D. (2021). Model-  
287 ing diurnal variation magnetic fields for mantle induction studies. *Geophysical*  
288 *Journal International*. doi: 10.1093/gji/ggaa533
- 289 Grayver, A., Kuvshinov, A., & Werthmüller, D. (2021). Time-domain model-  
290 ing of 3-D Earth's and planetary electromagnetic induction effect in ground  
291 and satellite observations. *Journal of Geophysical Research: Space Physics*,  
292 e2020JA028672. doi: 10.1029/2020JA028672
- 293 Grayver, A., Munch, F. D., Kuvshinov, A. V., Khan, A., Sabaka, T. J., & Tøffner-  
294 Clausen, L. (2017). Joint inversion of satellite-detected tidal and magne-  
295 toospheric signals constrains electrical conductivity and water content of the  
296 upper mantle and transition zone. *Geophysical Research Letters*, 44(12),  
297 6074–6081. doi: 10.1002/2017GL073446
- 298 Guzavina, M., Grayver, A., & Kuvshinov, A. (2019). Probing upper mantle elec-  
299 trical conductivity with daily magnetic variations using global to local trans-  
300 fer functions. *Geophysical Journal International*, 219(3), 2125–2147. doi:  
301 10.1093/gji/ggz412
- 302 Honkonen, I., Kuvshinov, A., Rastätter, L., & Pulkkinen, A. (2018). Predicting  
303 global ground geoelectric field with coupled geospace and three-dimensional  
304 geomagnetic induction models. *Space Weather*, 16(8), 1028–1041. doi:  
305 10.1029/2018SW001859
- 306 Ivannikova, E., Kruglyakov, M., Kuvshinov, A., Rastätter, L., & Pulkkinen, A.  
307 (2018). Regional 3-D modeling of ground electromagnetic field due to re-  
308 alistic geomagnetic disturbances. *Space Weather*, 16(5), 476–500. doi:  
309 10.1002/2017SW001793
- 310 Kelbert, A. (2020). The role of global/regional Earth conductivity models in natu-  
311 ral geomagnetic hazard mitigation. *Surveys in Geophysics*, 41, 115–166. doi:  
312 10.1007/s10712-019-09579-z
- 313 Korja, T., Engels, M., Zhamaletdinov, A. A., Kovtun, A. A., Palshin, N. A.,  
314 Smirnov, M. Y., ... BEAR Working Group (2002). Crustal conductiv-  
315 ity in Fennoscandia – a compilation of a database on crustal conductance  
316 in the Fennoscandian Shield. *Earth, Planets and Space*, 54, 535–558. doi:  
317 10.1186/BF03353044
- 318 Kruglyakov, M., & Kuvshinov, A. (2018). Using high-order polynomial basis in 3-D  
319 EM forward modeling based on volume integral equation method. *Geophysical*  
320 *Journal International*, 213(2), 1387–1401. doi: 10.1093/gji/ggy059
- 321 Kuvshinov, A., Grayver, A., Tøffner-Clausen, L., & Olsen, N. (2021). Probing 3-D  
322 electrical conductivity of the mantle using 6 years of Swarm, CryoSat-2 and  
323 observatory magnetic data and exploiting matrix Q-responses approach. *Earth,*  
324 *Planets and Space*, 73, 67. doi: 10.1186/s40623-020-01341-9
- 325 Love, J. J., Lucas, G. M., Kelbert, A., & Bedrosian, P. A. (2018). Geoelectric haz-  
326 ard maps for the Mid-Atlantic United States: 100 year extreme values and  
327 the 1989 magnetic storm. *Geophysical Research Letters*, 45(1), 5–14. doi:  
328 10.1002/2017GL076042
- 329 Marshalko, E., Kruglyakov, M., Kuvshinov, A., Juusola, L., Kwagala, N. K.,  
330 Sokolova, E., & Pilipenko, V. (2021). Comparing three approaches to  
331 the inducing source setting for the ground electromagnetic field modeling  
332 due to space weather events. *Space Weather*, 19(2), e2020SW002657. doi:  
333 10.1029/2020SW002657
- 334 Marshalko, E., Kruglyakov, M., Kuvshinov, A., Murphy, B. S., Rastätter, L., Ng-  
335 wira, C., & Pulkkinen, A. (2020). Exploring the influence of lateral con-  
336 ductivity contrasts on the storm time behavior of the ground electric field  
337 in the eastern United States. *Space Weather*, 18(3), e2019SW002216. doi:  
338 10.1029/2019SW002216

- 339 Pankratov, O., & Kuvshinov, A. (2016). Applied mathematics in EM stud-  
 340 ies with special emphasis on an uncertainty quantification and 3-D inte-  
 341 gral equation modelling. *Surveys in Geophysics*, *37*(1), 109–147. doi:  
 342 10.1007/s10712-015-9340-4
- 343 Püthe, C., & Kuvshinov, A. (2013). Towards quantitative assessment of the hazard  
 344 from space weather. Global 3-D modellings of the electric field induced by a  
 345 realistic geomagnetic storm. *Earth, Planets and Space*, *65*, 1017–1025. doi:  
 346 10.5047/eps.2013.03.003
- 347 Rosenqvist, L., & Hall, J. O. (2019). Regional 3-D modeling and verification of ge-  
 348 omagnetically induced currents in Sweden. *Space Weather*, *17*(1), 27–36. doi:  
 349 10.1029/2018SW002084
- 350 Sun, J., & Egbert, G. D. (2012). Spherical decomposition of electromagnetic fields  
 351 generated by quasi-static currents. *GEM - International Journal on Geomathe-*  
 352 *matics*, *3*(2), 279–295. doi: 10.1007/s13137-012-0039-0
- 353 Svetov, B. S. (1991). Transfer functions of the electromagnetic field (in Russian).  
 354 *Fizika Zemli*, *1*, 119–128.
- 355 Tanskanen, E. I. (2009). A comprehensive high-throughput analysis of sub-  
 356 storms observed by IMAGE magnetometer network: Years 1993–2003 ex-  
 357 amined. *Journal of Geophysical Research: Space Physics*, *114*(A5). doi:  
 358 10.1029/2008JA013682
- 359 Tasistro-Hart, A., Grayver, A., & Kuvshinov, A. (2021). Probabilistic geomagnetic  
 360 storm forecasting via deep learning. *Journal of Geophysical Research: Space*  
 361 *Physics*, *126*(1), e2020JA028228. doi: 10.1029/2020JA028228
- 362 Vanhamäki, H., & Juusola, L. (2020). Introduction to Spherical Elementary Current  
 363 Systems. In M. W. Dunlop & H. Lüher (Eds.), *Ionospheric multi-spacecraft*  
 364 *analysis tools: Approaches for deriving ionospheric parameters* (pp. 5–33).  
 365 Cham: Springer International Publishing. doi: 10.1007/978-3-030-26732-2\_2
- 366 Werthmüller, D., Key, K., & Slob, E. C. (2019). A tool for designing digital filters  
 367 for the Hankel and Fourier transforms in potential, diffusive, and wavefield  
 368 modeling. *Geophysics*, *84*(2), F47–F56. doi: 10.1190/geo2018-0069.1
- 369 Zenhausern, G., Kuvshinov, A., Guzavina, M., & Maute, A. (2021). Towards prob-  
 370 ing Earth’s upper mantle with daily magnetic field variations: exploring a  
 371 physics-based parametrization of the source. *Earth, Planets and Space*, *73*,  
 372 136. doi: 10.1186/s40623-021-01455-8

## 373 Appendix A Properties of transfer functions and impulse responses

374 The convolution integrals in Equation (9) represent the response of the medium  
 375 to a time-varying extraneous current. These relations follow from the properties of a phys-  
 376 ical system we consider. We list these properties below and discuss implications. The  
 377 presentation closely follows a more detailed analysis by Svetov (1991). Note that for the  
 378 sake of clarity, we discuss the properties on an example of abstract scalar quantities and  
 379 omit their dependence on spatial variables and electrical conductivity pertinent to our  
 380 application.

1. **Linearity** allows us to define a response,  $\zeta(t)$ , of the medium at time  $t$  to an ex-  
 traneous forcing as

$$\zeta(t) = \int_{-\infty}^{\infty} \mathcal{F}(t, t') \chi(t') dt', \quad (\text{A1})$$

381 where  $\chi$  is the extraneous forcing that depends on time  $t'$  and  $\mathcal{F}(t, t')$  is the medium  
 382 Green’s function.

2. **Stationarity** implies that the response of the medium does not depend on the  
 time of occurrence of the excitation. In this case  $\mathcal{F}(t, t') \equiv f(t-t')$  and eq. (A1)

is rewritten as a convolution integral

$$\zeta(t) = \int_{-\infty}^{\infty} f(t-\tau)\chi(\tau)d\tau = \int_{-\infty}^{\infty} f(\tau)\chi(t-\tau)d\tau, \quad (\text{A2})$$

where  $f(t)$  represents the impulse response of the medium. In the frequency domain, the convolution integral degenerates to

$$\tilde{\zeta}(\omega) = \tilde{f}(\omega)\tilde{\chi}(\omega), \quad (\text{A3})$$

where  $\tilde{f}(\omega)$  is called the transfer function and we use tilde sign ( $\tilde{\cdot}$ ) to denote complex-valued quantities. Equations (A2) and (A3) are related through the Fourier transform

$$\tilde{f}(\omega) = \int_{-\infty}^{\infty} f(t)e^{i\omega t}dt. \quad (\text{A4})$$

- 383 3. Since we work in the time domain with a real-valued forcing, the impulse response  
 384 is also **real**. To see implications of this, let us define the inverse Fourier transform  
 385 of  $\tilde{f}(\omega) = f_R(\omega) + if_I(\omega)$  as

$$\begin{aligned} f(t) &= \frac{1}{2\pi} \int_{-\infty}^{\infty} \tilde{f}(\omega)e^{-i\omega t}d\omega \\ &= \frac{1}{2\pi} \int_{-\infty}^{\infty} [f_R(\omega)\cos(\omega t) + f_I(\omega)\sin(\omega t)]d\omega \\ &\quad + \frac{i}{2\pi} \int_{-\infty}^{\infty} [f_I(\omega)\cos(\omega t) - f_R(\omega)\sin(\omega t)]d\omega, \end{aligned} \quad (\text{A5})$$

386 For an impulse response to be real, the last term in the integral (A5) has to van-  
 387 ish. This is possible only if  $f_R(\omega)$  and  $f_I(\omega)$  are even and odd functions of  $\omega$ , re-  
 388 spectively. Therefore, Equation (A5) reduces to

$$f(t) = \frac{1}{\pi} \int_0^{\infty} [f_R(\omega)\cos(\omega t) + f_I(\omega)\sin(\omega t)]d\omega. \quad (\text{A6})$$

4. Impulse response is **causal**. This property implies that  $f(t) = 0$  for  $t < 0$ . Under this assumption, the convolution integral (A2) is recast to

$$\zeta(t) = \int_0^{\infty} f(\tau)\chi(t-\tau)d\tau = \int_{-\infty}^t f(t-\tau)\chi(\tau)d\tau. \quad (\text{A7})$$

Due to causality and exploiting Equation (A6), the impulse response is determined by using either only real or imaginary part of  $\tilde{f}(\omega)$ :

$$f(\tau) = \frac{2}{\pi} \int_0^{\infty} f_R(\omega)\cos(\omega\tau)d\omega = -\frac{2}{\pi} \int_0^{\infty} f_I(\omega)\sin(\omega\tau)d\omega. \quad (\text{A8})$$

## 389 Appendix B Details of the numerical computation of the real-time GEF

As discussed in the main text, to calculate the GEF in near-real time one needs to efficiently estimate integrals in the right-hand side (RHS) of the equation below

$$\mathbf{E}(\mathbf{r}_s, t; \sigma) = \sum_{i=1}^L \int_0^{\infty} c_i(t-\tau)\mathbf{E}_i(\mathbf{r}_s, \tau; \sigma)d\tau \approx \sum_{i=1}^L \int_0^T c_i(t-\tau)\mathbf{E}_i(\mathbf{r}_s, \tau; \sigma)d\tau. \quad (\text{B1})$$

With finite  $T$ , one must account for a possibly substantial linear trend in time series  $c_i(t)$ . By removing the trend, we are forced to work with the following function

$$d_i(t, \tau; T) = \begin{cases} c_i(t - \tau) - c_i(t) - \frac{c_i(t - T) - c_i(t)}{T} \tau, & \tau \in [0, T] \\ 0, & \tau \notin [0, T]. \end{cases} \quad (\text{B2})$$

Substituting Equation (B2) into the RHS of Equation (B1), and considering (for simplicity) only one term in the sum, we obtain

$$\begin{aligned} \int_0^T c_i(t - \tau) \mathbf{E}_i(\mathbf{r}_s, \tau; \sigma) d\tau &= c_i(t) \int_0^T \mathbf{E}_i(\mathbf{r}_s, \tau; \sigma) d\tau + \\ \int_0^T d_i(t, \tau; T) \mathbf{E}_i(\mathbf{r}_s, \tau; \sigma) d\tau &+ \frac{c_i(t - T) - c_i(t)}{T} \int_0^T \tau \mathbf{E}_i(\mathbf{r}_s, \tau; \sigma) d\tau. \end{aligned} \quad (\text{B3})$$

Recall that  $T$  should be taken large enough to make approximation (B1) valid; particularly, this means that

$$\int_0^T \mathbf{E}_i(\mathbf{r}_s, \tau; \sigma) d\tau \approx \int_0^\infty \mathbf{E}_i(\mathbf{r}_s, \tau; \sigma) d\tau. \quad (\text{B4})$$

But the integral in the RHS of the latter equation is zero since it corresponds to the electric field generated by the time-constant source. Then, Equation (B3) can be approximated as

$$\int_0^T c_i(t - \tau) \mathbf{E}_i(\mathbf{r}_s, \tau; \sigma) d\tau \approx \int_0^T d_i(t, \tau; T) \mathbf{E}_i(\mathbf{r}_s, \tau; \sigma) d\tau + [c_i(t - T) - c_i(t)] L_i(\mathbf{r}_s, T; \sigma), \quad (\text{B5})$$

where

$$L_i(\mathbf{r}_s, T; \sigma) = \frac{1}{T} \int_0^T \tau \mathbf{E}_i(\mathbf{r}_s, \tau; \sigma) d\tau. \quad (\text{B6})$$

390 The integrals  $L_i(\mathbf{r}_s, T; \sigma)$  can be computed using the digital filter technique (see Appendix  
391 C), whereas first term in the RHS of Equation (B5) is estimated as follows.

Taking into account that we have  $c_i(t)$  at discrete time instants,  $t = n\Delta t$ ,  $n = 0, 1, \dots$ , we approximate  $d_i(t, \tau; T)$  using the Whittaker-Shannon (sinc) interpolation formula

$$d_i(t, \tau; T) \approx \sum_{n=0}^{n\Delta t \leq T} d_i(t, n\Delta t; T) \text{sinc} \frac{\tau - n\Delta t}{\Delta t}, \quad (\text{B7})$$

where

$$\text{sinc}(x) = \frac{\sin \pi x}{\pi x}. \quad (\text{B8})$$

Recall that sinc interpolation is a method to construct a continuous band-limited function from a sequence of real numbers, in our case time series  $d_i$  at time instants  $t = n\Delta t$ ,  $n = 0, 1, \dots$ . Note that in our context, the term ‘‘band-limited function’’ means that non-zero values of a Fourier transform of this function are confined to the frequencies

$$|\omega| \leq \frac{\pi}{\Delta t}. \quad (\text{B9})$$

Using the approximation (B7) and taking into account that  $\mathbf{E}_i(\mathbf{r}_s, \tau; \sigma) = 0$ ,  $\tau < 0$  (cf. Appendix A), one obtains

$$\int_0^T d_i(t, \tau; T) \mathbf{E}_i(\mathbf{r}_s, \tau; \sigma) d\tau \approx \int_0^\infty d_i(t, \tau; T) \mathbf{E}_i(\mathbf{r}_s, \tau; \sigma) d\tau = \quad (\text{B10})$$

$$\int_{-\infty}^{\infty} d_i(t, \tau; T) \mathbf{E}_i(\mathbf{r}_s, \tau; \sigma) d\tau = \sum_{n=0}^{n\Delta t \leq T} d_i(t, n\Delta t; T) \int_{-\infty}^{\infty} \mathbf{E}_i(\mathbf{r}_s, \tau; \sigma) \operatorname{sinc} \frac{\tau - n\Delta t}{\Delta t} d\tau.$$

Thus, we can write

$$\int_0^T d_i(t, \tau; T) \mathbf{E}_i(\mathbf{r}_s, \tau; \sigma) d\tau = \sum_{n=0}^{n\Delta t \leq T} d_i(t, n\Delta t; T) G_{\mathbf{E}_i}^n(\mathbf{r}_s; \sigma), \quad (\text{B11})$$

where

$$G_{\mathbf{E}_i}^n(\mathbf{r}_s; \sigma) = \int_{-\infty}^{\infty} \mathbf{E}_i(\mathbf{r}_s, \tau; \sigma) \operatorname{sinc} \frac{\tau - n\Delta t}{\Delta t} d\tau. \quad (\text{B12})$$

Further, following the properties of the Fourier transform as applied to sinc function, we obtain that

$$G_{\mathbf{E}_i}^n(\mathbf{r}_s; \sigma) = \frac{\Delta t}{2\pi} \int_{-\frac{\pi}{\Delta t}}^{\frac{\pi}{\Delta t}} \mathbf{E}_i(\mathbf{r}_s, \omega; \sigma) e^{-i\omega n\Delta t} d\omega = \operatorname{Re} \left\{ \frac{\Delta t}{\pi} \int_0^{\frac{\pi}{\Delta t}} \mathbf{E}_i(\mathbf{r}_s, \omega; \sigma) e^{-i\omega n\Delta t} d\omega \right\}. \quad (\text{B13})$$

Finally, substituting Equation (B11) in Equation (B5), and (B5) in the RHS of (B1) we obtain Equation (11)

$$\mathbf{E}(\mathbf{r}_s, t_k; \sigma) \approx \sum_{i=1}^L \left\{ \sum_{n=0}^{N_t} d_i(t_k, n\Delta t; T) G_{\mathbf{E}_i}^n(\mathbf{r}_s; \sigma) + [c_i(t_k - T) - c_i(t_k)] L_i(\mathbf{r}_s, T; \sigma) \right\},$$

392 where  $d_i(t_k, n\Delta t; T)$ ,  $L_i(\mathbf{r}_s, T; \sigma)$ , and  $G_{\mathbf{E}_i}^n(\mathbf{r}_s; \sigma)$  are defined in Equations (B2)), (B6)  
 393 and (B13), respectively. Note that the estimation of the integral in the RHS of Equa-  
 394 tion (B13) is performed using a suitable quadrature formula.

395 An important note here is that, according to (B13), one does not need to compute  
 396  $\mathbf{E}_i(\mathbf{r}_s, \omega; \sigma)$  for  $\omega > \frac{\pi}{\Delta t}$ . This may be obvious, however, this is not the case if one uses  
 397 piece-wise constant (PWC) approximation of  $c_i(t)$  as it is done, for example, in Grayver  
 398 et al. (2021). With PWC approximation, one is forced to compute the fields at very high  
 399 frequencies irrespective of  $\Delta t$  value; this can pose a problem from the numerical point  
 400 of view.

## 401 Appendix C Computation of $L_i(\mathbf{r}_s, T; \sigma)$

With the use of Equation (A8),  $\mathbf{E}_i(\mathbf{r}_s, \tau; \sigma)$  can be written as

$$\mathbf{E}_i(\mathbf{r}_s, \tau; \sigma) = -\frac{2}{\pi} \int_0^{\infty} \operatorname{Im} \mathbf{E}_i(\mathbf{r}_s, \omega; \sigma) \sin(\omega\tau) d\omega. \quad (\text{C1})$$

Substituting the latter equation into Equation (B6) and rearranging the order of inte-  
 gration, we write  $L_i(\mathbf{r}_s, T; \sigma)$  in the following form

$$L_i(\mathbf{r}_s, T; \sigma) = T \int_0^{\infty} \Phi(\omega T) \operatorname{Im} \mathbf{E}_i(\mathbf{r}_s, \omega; \sigma) d\omega, \quad (\text{C2})$$

where  $\Phi(\omega T)$  reads

$$\Phi(\omega T) = -\frac{2}{\pi} \frac{1}{T^2} \int_0^T \tau \sin(\omega\tau) d\tau = -\frac{2}{\pi} \left[ \frac{\sin(\omega T)}{(\omega T)^2} - \frac{\cos(\omega T)}{\omega T} \right]. \quad (\text{C3})$$

Integrals in (C2) can be efficiently estimated using the digital filter technique. Specifically, one needs to construct a digital filter for the following integral transform

$$F(T) = T \int_0^{\infty} \Phi(\omega T) f(\omega) d\omega. \quad (\text{C4})$$

To obtain filter's coefficients for this transform, we exploit the same procedure as in Werthmüller et al. (2019) using the following pair of output and input functions

$$\begin{aligned} F(T) &= \frac{(T+1)e^{-T} - 1}{T}, \\ f(\omega) &= \frac{\omega}{1 + \omega^2}. \end{aligned} \quad (\text{C5})$$

402

## Appendix D Formulas for $P$ and $Q$

The formulas for  $P(\mathbf{r}, \mathbf{r}_m)$  and  $Q(\mathbf{r}, \mathbf{r}_m)$  (in slightly different notations) are taken from Vanhamäki and Juusola (2020) (see their Sections 2.3 and 2.5) and are as follows

$$P(\mathbf{r}, \mathbf{r}_m) = \frac{\sin C}{4\pi R} \cot \frac{\gamma}{2}, \quad (\text{D1})$$

$$Q(\mathbf{r}, \mathbf{r}_m) = \frac{\cos C}{4\pi R} \cot \frac{\gamma}{2}, \quad (\text{D2})$$

where  $R = a + h$ ,  $\mathbf{r} = (R, \vartheta, \varphi)$ ,  $\mathbf{r}_m = (R, \vartheta_m, \varphi_m)$  and  $\gamma$  is an angle between  $\mathbf{r}$  and  $\mathbf{r}_m$ ;  $\gamma$  can be determined from the following spherical trigonometry formula

$$\cos \gamma = \cos \vartheta \cos \vartheta_m + \sin \vartheta \sin \vartheta_m \cos(\varphi - \varphi_m), \quad (\text{D3})$$

and  $\cos C$  and  $\sin C$  are given as

$$\cos C = \frac{\cos \vartheta_m - \cos \vartheta \cos \gamma}{\sin \vartheta \sin \gamma}, \quad (\text{D4})$$

$$\sin C = \frac{\sin \vartheta_m \sin(\varphi_m - \varphi)}{\sin \gamma}. \quad (\text{D5})$$

403

404

405

406

From Equations (D1) and (D2), it is seen that  $P(\mathbf{r}, \mathbf{r}_m)$  and  $Q(\mathbf{r}, \mathbf{r}_m)$  tend to infinity as  $\mathbf{r}$  tends to  $\mathbf{r}_m$ . The simplest way to deal with this issue is, as mentioned in Vanhamäki and Juusola (2020), is to consider the grids for  $\mathbf{r}$  and  $\mathbf{r}_m$  that are shifted with respect to each other. This approach is used in the current paper.

**Table 1.** Normalized root-mean-square errors and correlation coefficients between reference GEF components and GEF components simulated using real-time 3-D GEF modeling approach with 15 min and 1 h time segments at Abisko (ABK), Uppsala (UPS) and Saint Petersburg (SPG) geomagnetic observatories. The results are shown for a time window from 20:00:00 UT, 7 September 2017, to 03:59:50 UT, 8 September 2017.

	ABK	UPS	SPG
nRMSE( $E_{x,\text{orig}}, E_{x,15\text{min}}$ )	0.286	0.188	0.205
nRMSE( $E_{x,\text{orig}}, E_{x,1\text{h}}$ )	0.279	0.139	0.14
nRMSE( $E_{y,\text{orig}}, E_{y,15\text{min}}$ )	0.271	0.163	0.268
nRMSE( $E_{y,\text{orig}}, E_{y,1\text{h}}$ )	0.278	0.122	0.182
corr( $E_{x,\text{orig}}, E_{x,15\text{min}}$ )	0.984	0.991	0.989
corr( $E_{x,\text{orig}}, E_{x,1\text{h}}$ )	0.984	0.995	0.995
corr( $E_{y,\text{orig}}, E_{y,15\text{min}}$ )	0.985	0.993	0.983
corr( $E_{y,\text{orig}}, E_{y,1\text{h}}$ )	0.979	0.997	0.992

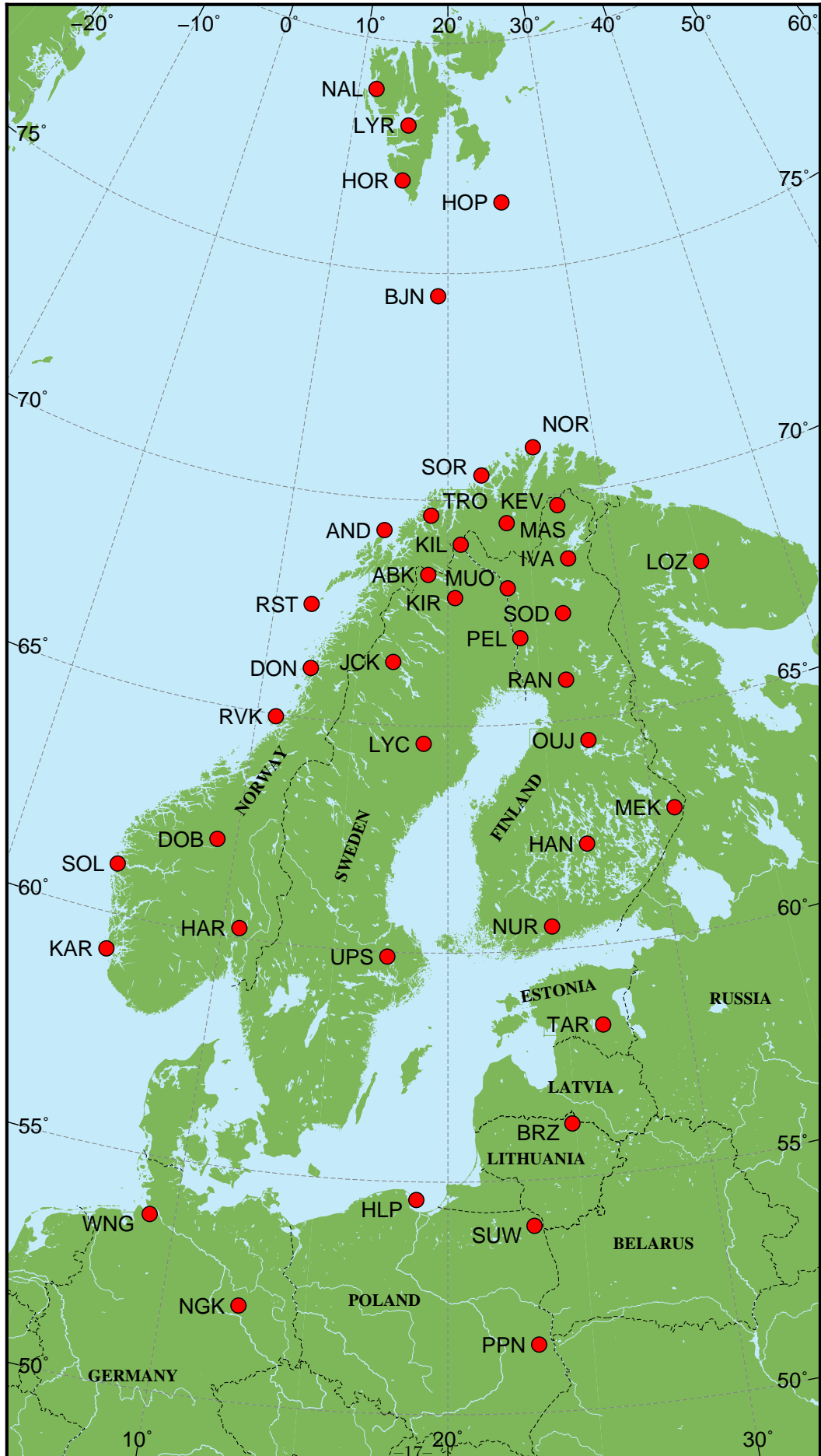


**Figure 1.** Location of IMAGE magnetometer network. Credit: Finnish Meteorological Institute.

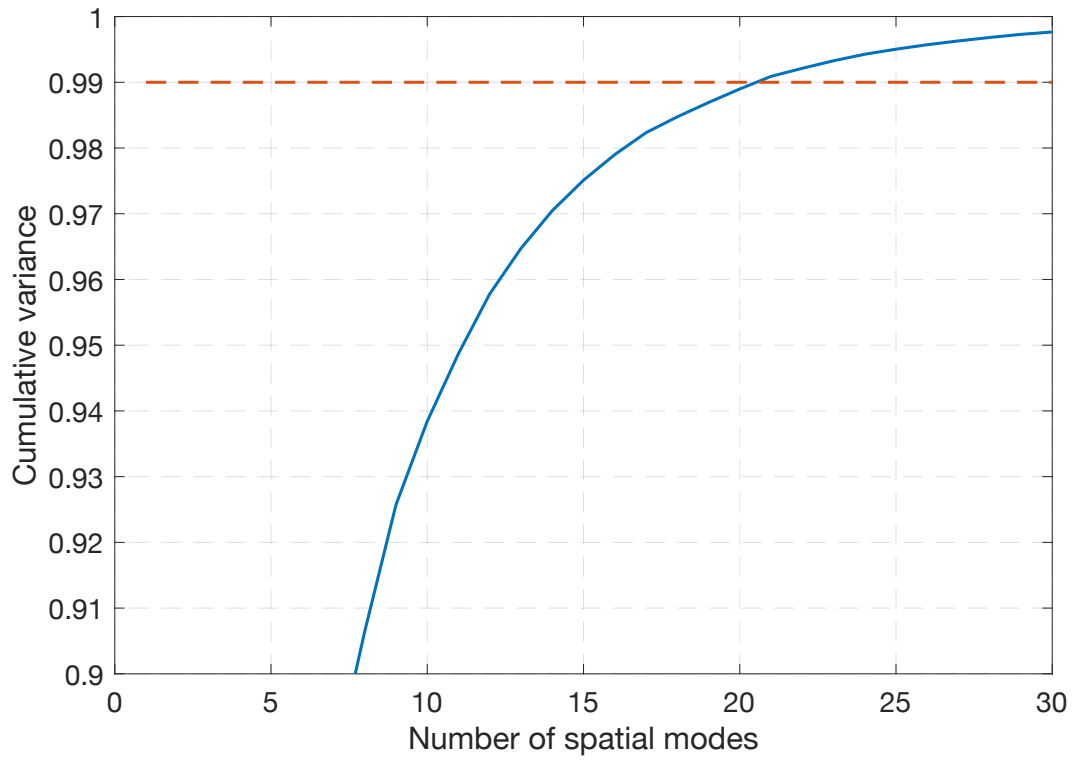


**Figure 2.** Cumulative variance for the first 30 spatial modes. Dashed line marks the 99 % threshold.

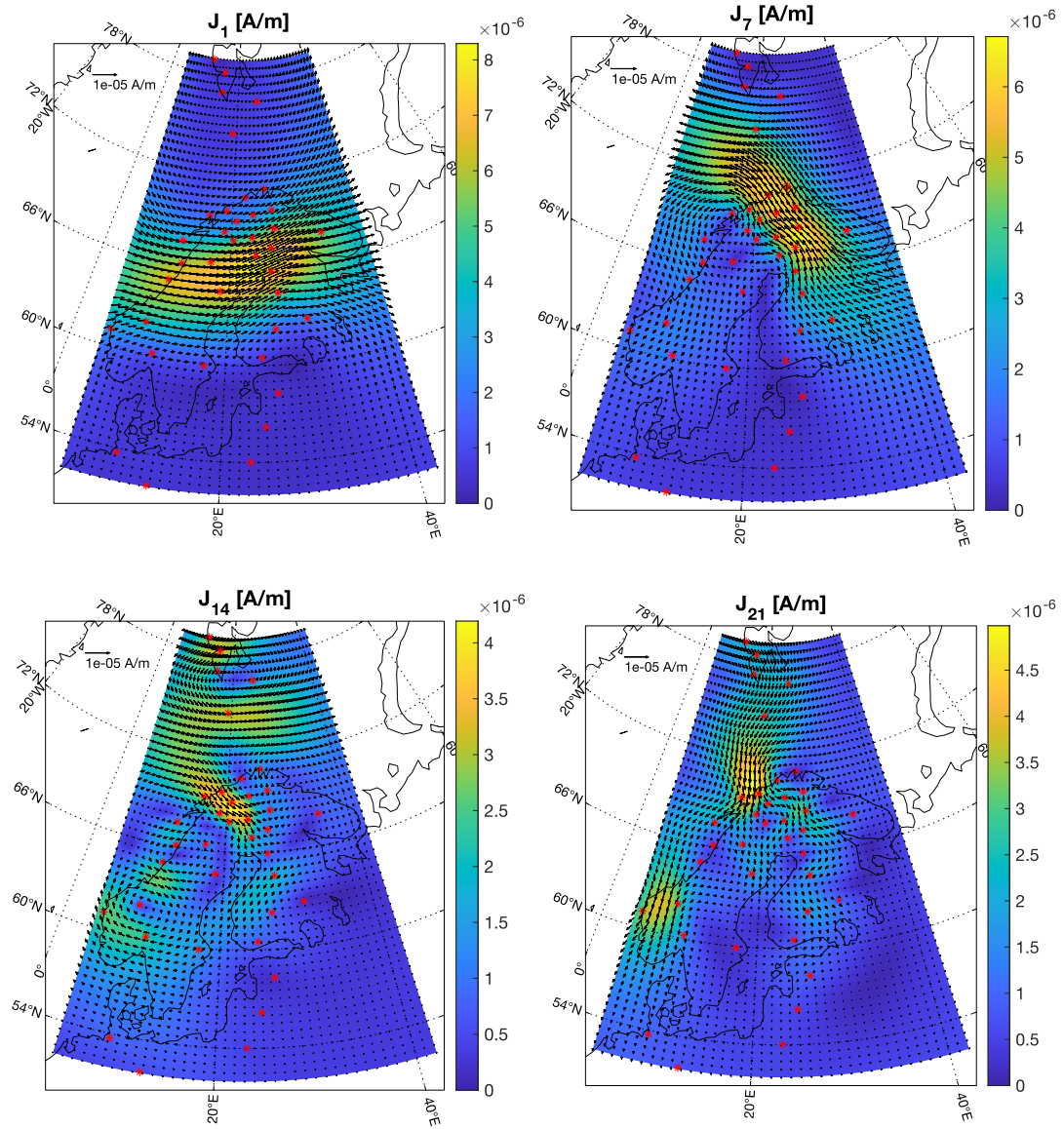


**Figure 3.** A selection of PCA-recovered  $J_i$ ,  $i = 1, 7, 14, 21$ . See details in the text.

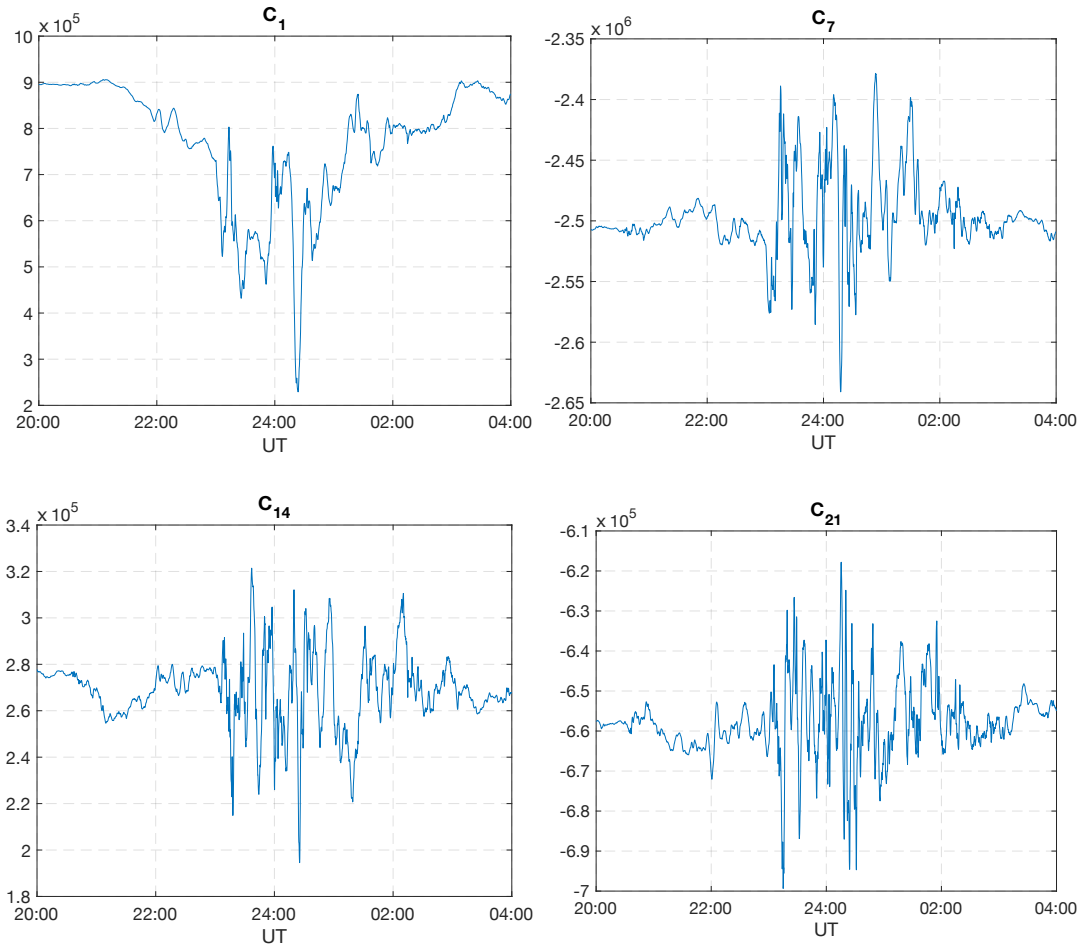


**Figure 4.** A selection of PCA-recovered  $c_i$ ,  $i = 1, 7, 14, 21$ . See details in the text.

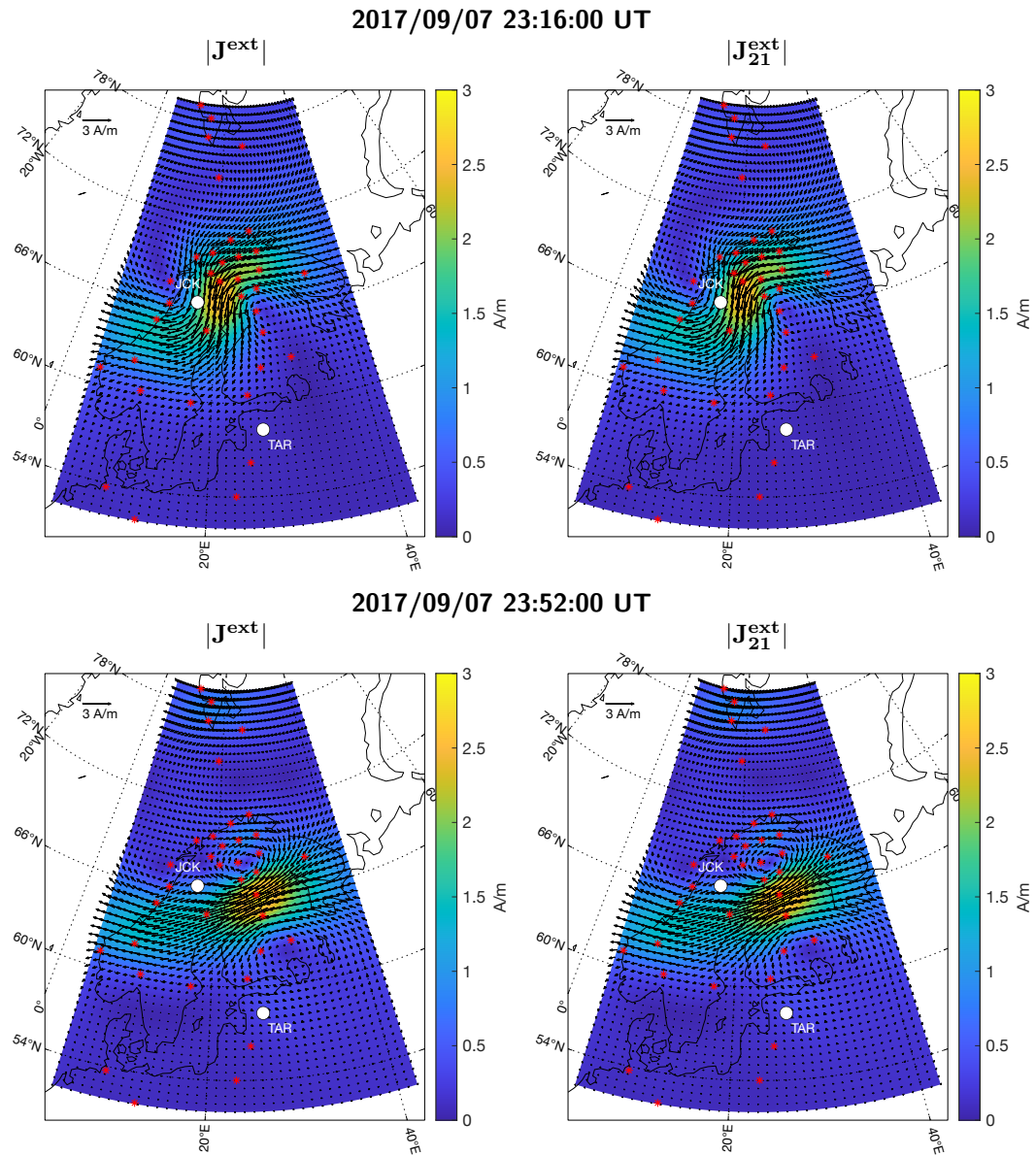


**Figure 5.** Left: the original external equivalent current; right: the external equivalent current constructed using 21 spatial modes. The results are for two time instants: 23:16:00 and 23:52:00 UT on September 7, 2017.

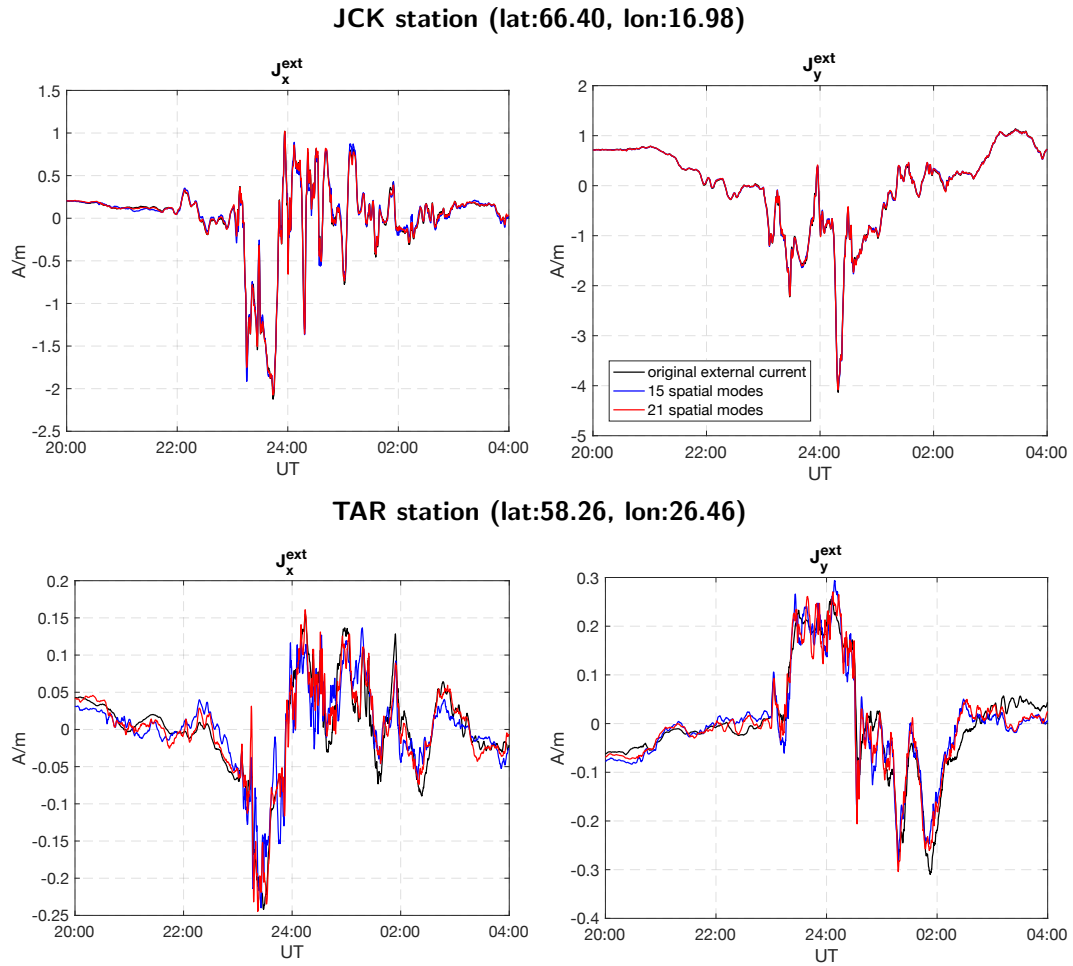


**Figure 6.** Time series of the original external equivalent current (black curves) and external equivalent current constructed using 15 (blue curves) and 21 spatial modes (red curves) above two exemplary sites (Jäckvik (JCK) and Tartu (TAR)). Locations of the sites are shown in Figure 5 as white circles.

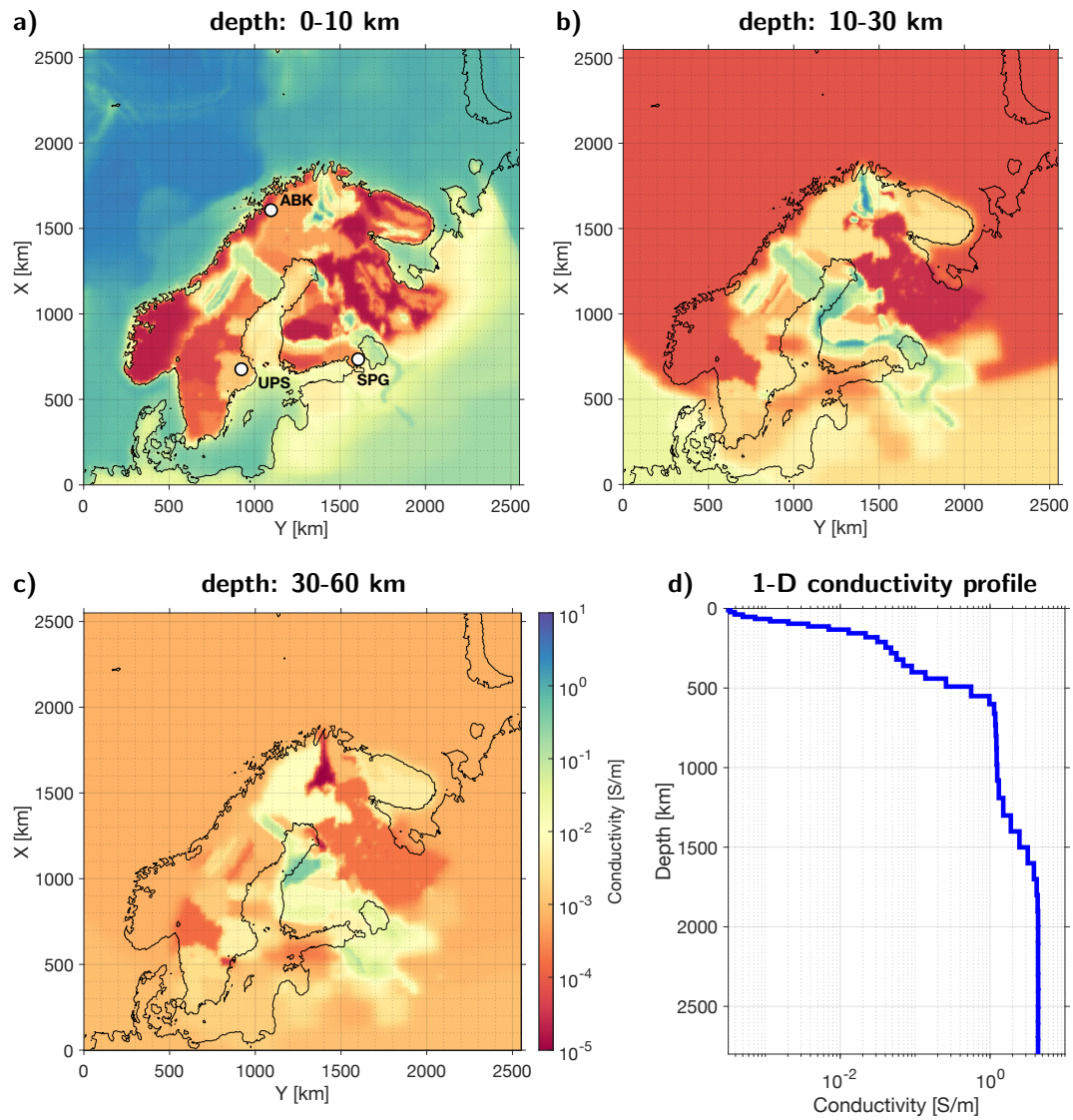


**Figure 7.** Conductivity distribution [S/m] in the model of Fennoscandia: (a)–(c) Plane view on 3 layers of the 3-D part of the model; (d) global 1-D conductivity profile from Kuvshinov et al. (2021) used in this study. Locations of geomagnetic observatories Abisko (ABK), Uppsala (UPS), and Saint Petersburg (SPG) are marked with circles in plot (a).

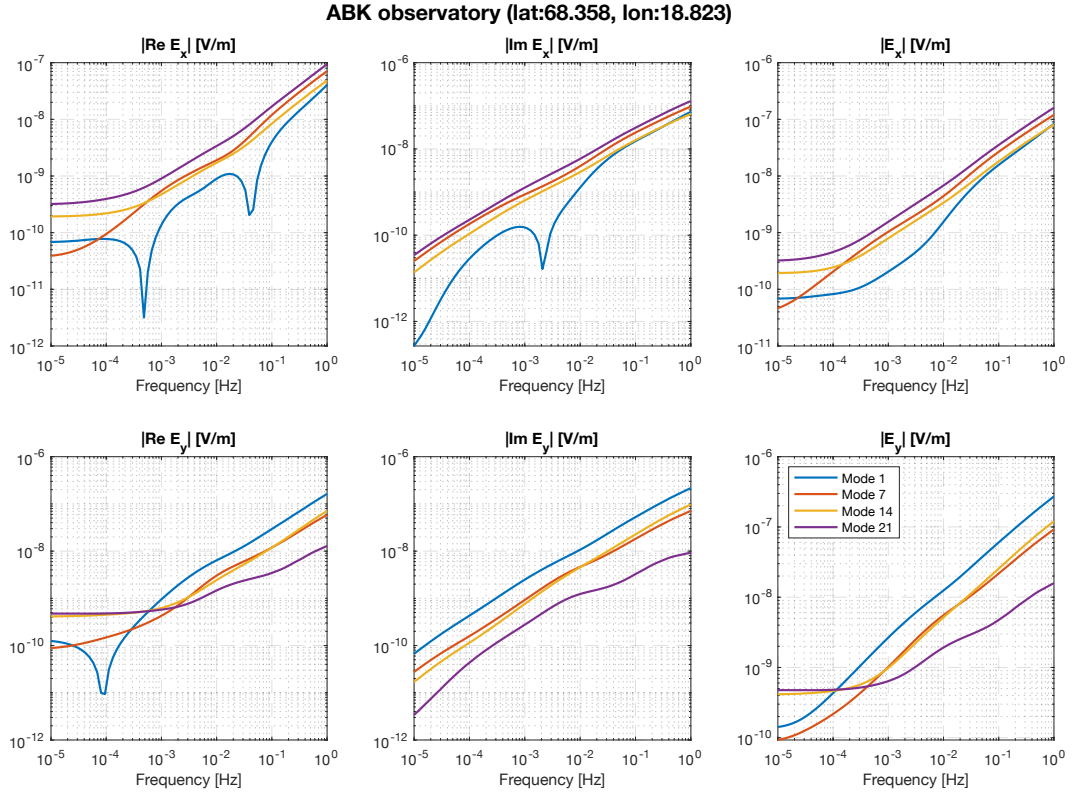


**Figure 8.** From left to right: absolute values of real part, imaginary part and magnitude of  $\mathbf{E}_i(\mathbf{r}_s, \omega; \sigma)$  with respect to frequency, and for a number of spatial modes. Results are for observatory Abisko (ABK) located near the seashore (cf. Fig. 7a). Top and bottom rows show the results for  $E_{x,i}$  and  $E_{y,i}$  components, respectively.

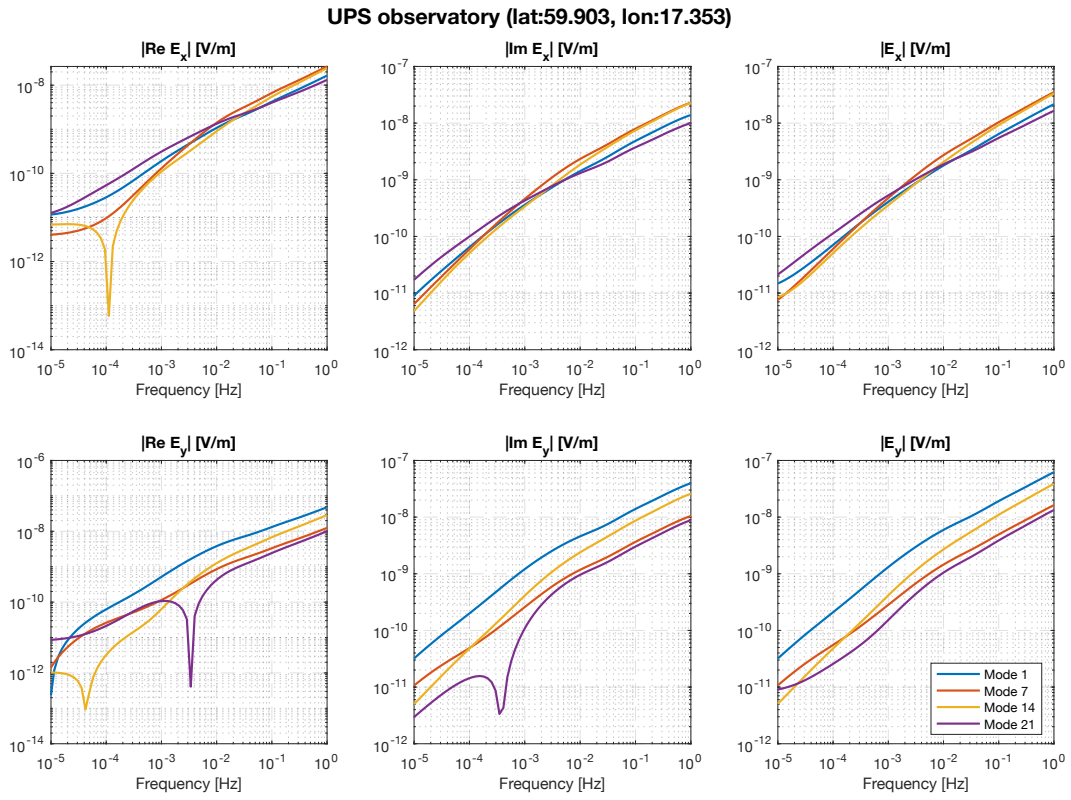


**Figure 9.** The same caption as in Figure 8 but for inland, Uppsala (UPS), geomagnetic observatory.

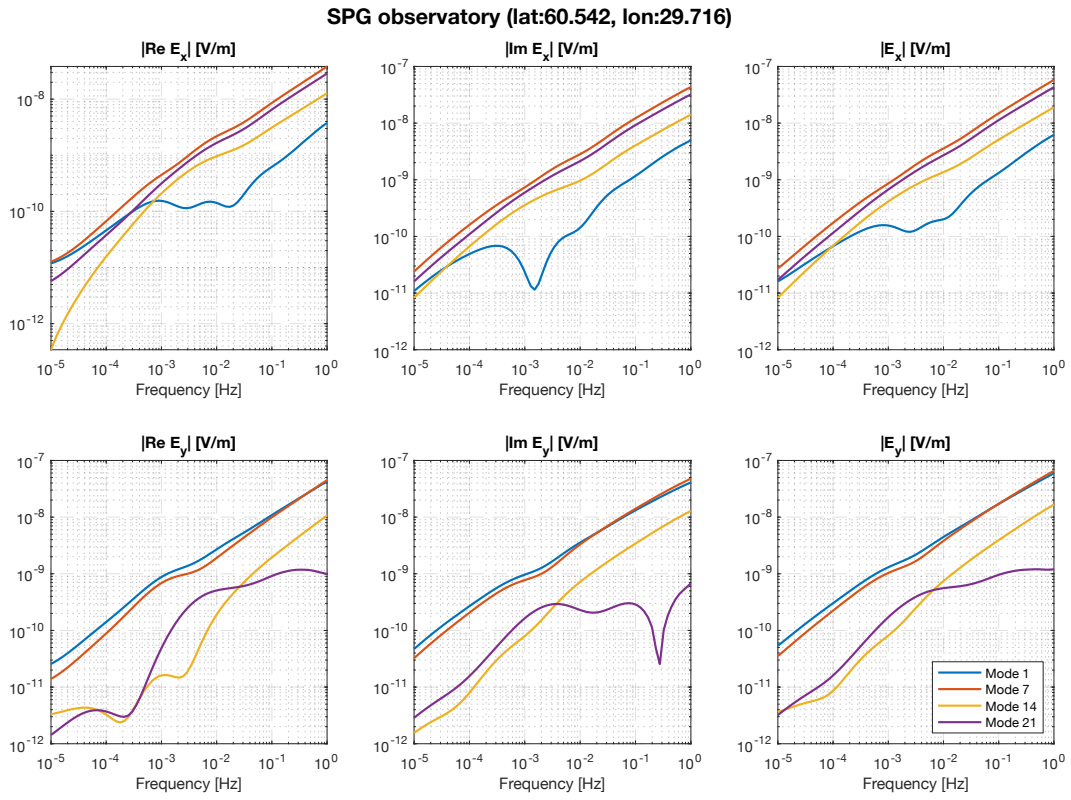


**Figure 10.** The same caption as in Figure 8 but for Saint Petersburg (SPG) geomagnetic observatory.

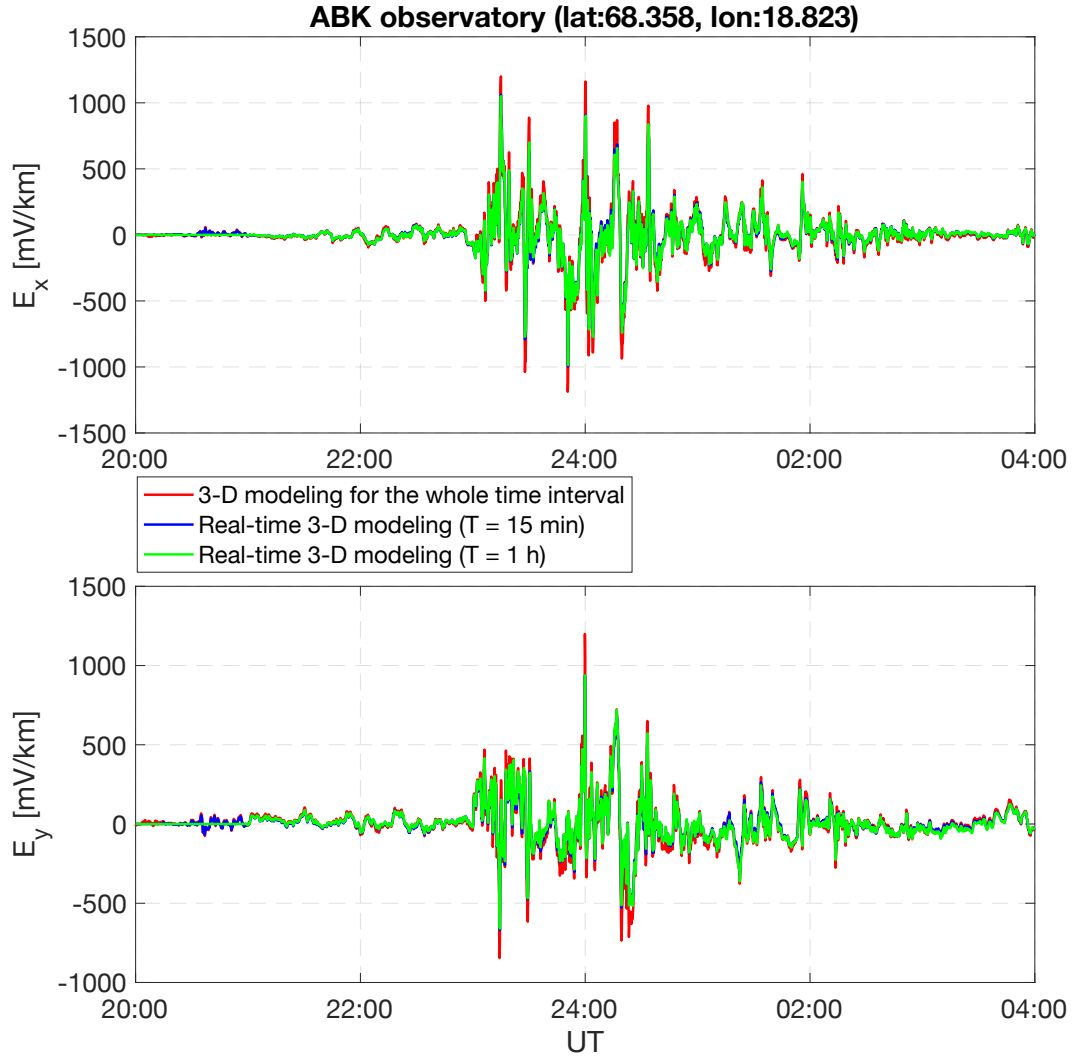


**Figure 11.** Electric field components at Abisko (ABK) geomagnetic observatory location obtained using 3-D EM modeling with 21 spatial modes for the whole 8 h time interval (red curves) and electric field components at the same observatory simulated using real-time 3-D GEF modeling approach with 15 min (blue curves) and 1 h (green curves) time segments.

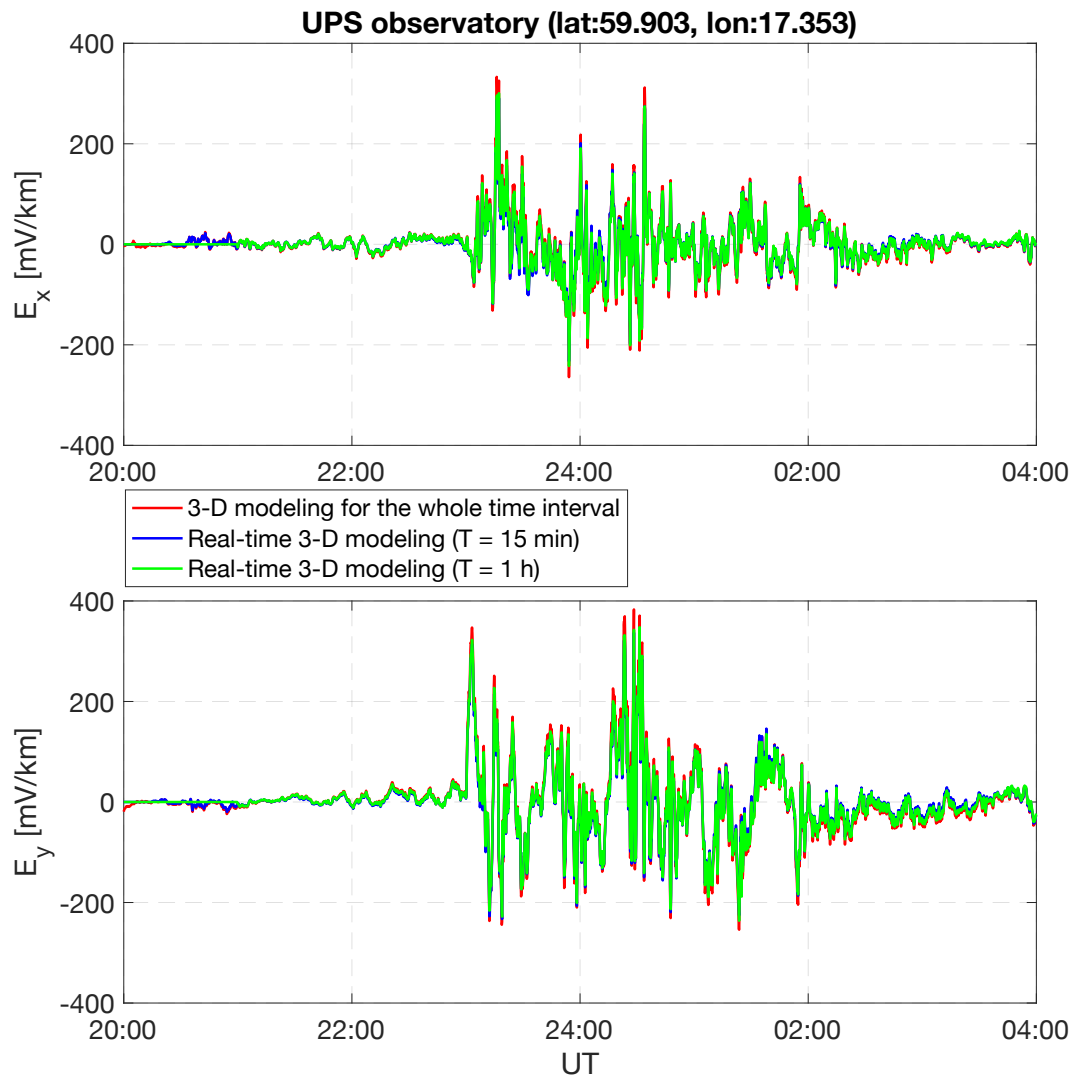


**Figure 12.** The same caption as in Figure 11 but for Uppsala (UPS) geomagnetic observatory.

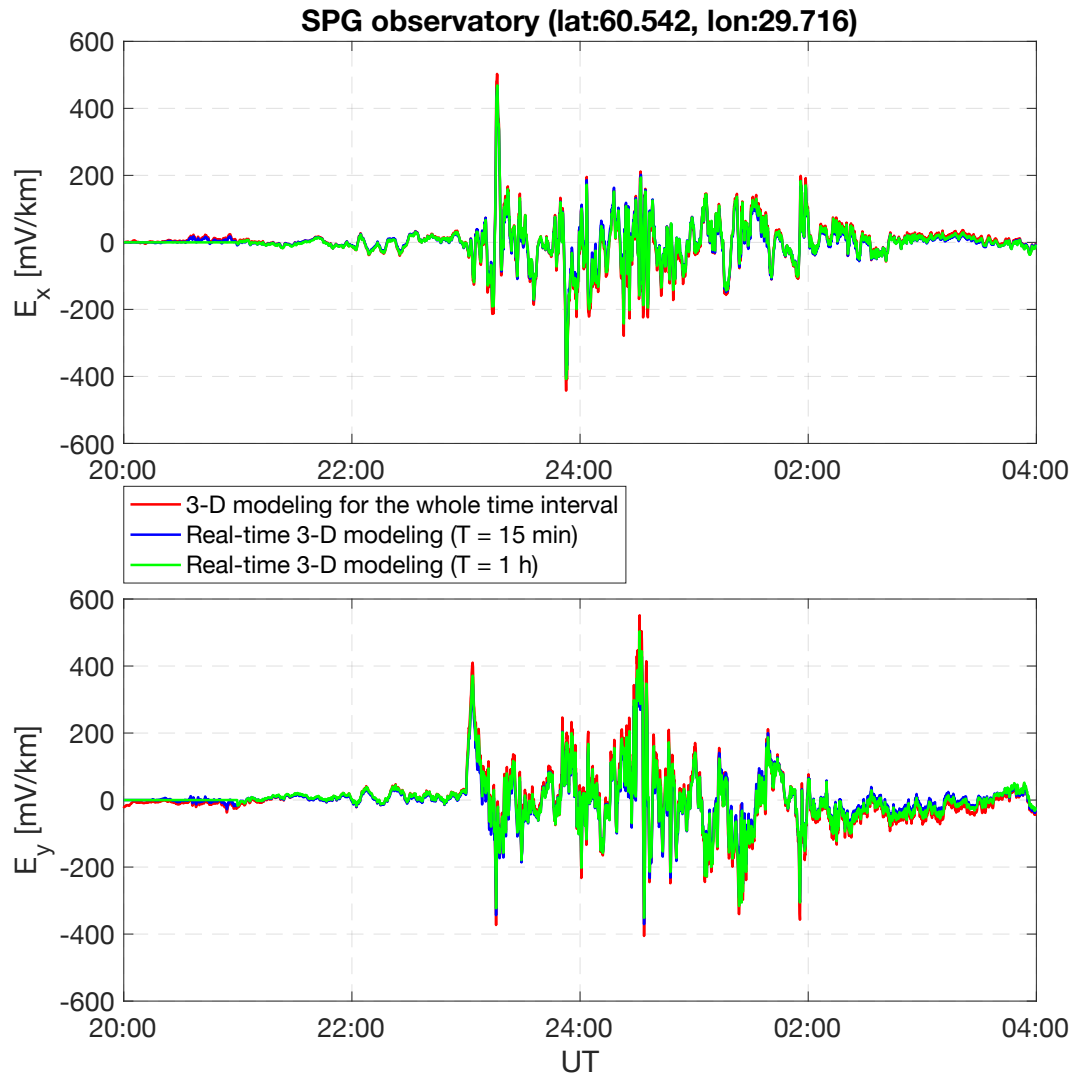


**Figure 13.** The same caption as in Figure 13 but for Saint Petersburg (SPG) geomagnetic observatory.